Supplementary Material Imaging the source region of Cascadia tremor and intermediate-depth earthquakes

A. Data Collection and Processing

The Cascadia Arrays For Earthscope (CAFE) experiment deployed 47 broadband seismometers from August 2006 to September 2008, although only data for the first 15 months were available for the analyses here. The seismographs, which were placed in shallow sand-filled mini-vaults, recorded broadband ground velocity with 120 s corner period at 50 samples per second. Most lie in a broad E-W swath near 47°N, with 5 km arc-normal spacing near the coast increasing to 25 km at the volcanic arc. Two sparser cross-lines provide three-dimensional control. CAFE data are integrated with EarthScope Transportable Array (TA) stations at 70 km spacing, operating concurrently, and with data from the Pacific Northwest Seismograph Network (PNSN), giving 79 usable stations. In addition, three 6-element small-aperture arrays provide constraints on sources of non-volcanic tremor, although most tremor locations shown in Figure 1 rely upon other arrays (Wech and Creager, 2008; Wech et al., 2008).

For teleseismic analyses, signals from 27 earthquakes met quality standards leading to 650 usable *P* waves (Figure 1, inset). All earthquakes have body-wave magnitude > 5.5, lie between 30° and 90° from the array, and produce easily visible signals at most stations; in addition, several checks were performed to ensure stability of deconvolutions, as described elsewhere (MacKenzie, 2008). All stations are used to isolate the scattered *SV* and *SH* wavefield, but only those in the cross arc swath are migrated. These criteria give an average of 17 earthquakes per station.

Local earthquakes in the PNSN catalog are relocated from the broadband arrays, from *P* and *S* arrivals identified using an auto-adaptive onset estimation scheme (Pisarenko et al., 1987). Tremor locations are measured with an automated cross-correlation method (Wech and Creager, 2008; Wech et al., 2008).

B. Imaging Method and Resolution

The scattered wavefield is extracted from *P* coda (Bostock and Rondenay, 1999; Rondenay et al., 2005). The *P* and *S* wavefields are isolated by an inverse free-surface transformation (Kennett, 1991) for a 90 second window starting just before the *P* onset, and then aligned by cross-correlating the *P* component (VanDecar and Crosson, 1990). The first eigenmode of the resulting wavefield image provides an estimate of the incident *P* wavefield, the first 30 to 50 s of which are then deconvolved from the *S* (*SV* and *SH*) and remaining, scattered *P* signals. The resulting scattered wavefield comprises the data set used for imaging, filtered between 0.3 and 0.03 Hz to reduce the effects of scattering from topography at the free-surface (Rondenay et al., 2005) and to avoid noisy signal components.

Images of velocity perturbations are constructed using multichannel inversion of scattered teleseismic body waves, assuming two-dimensional velocity variations (Bostock et al., 2001). The method assumes the single-scattering Born approximation, and includes both the forward-scattered or direct *P*-to-*S* conversion (*Ps*) as well as back-scattered, surface-reflected modes *(Ppxs*, *Psxs*) in estimating variations in *Vs*, the *S*-wave velocity structure. The *P*-velocity image relies only upon the surface-reflected, back-scattered *P* mode (*Ppxp*). Fractional velocity perturbations, expressed as d*Vs/Vs* or d*Vp/Vp*, are calculated relative to the one-dimensional velocity model used to trace rays (Supplementary Table S1). That model is primarily taken from that used to locate earthquakes in the Puget Sound region (Ludwin, 1994) by assuming *Vp/Vs*=1.75, although several alternatives have been tested (MacKenzie, 2008). Based on dip and image sharpness tests and the local trend of the Cascades volcanic arc, the image is projected at a cross-section azimuth of 100° (i.e., rotated 10° clockwise from E-W). The images (Figure 2) have been muted for depths less than 9 km, where spatial aliasing may occur (Rondenay et al., 2005).

The surface-reflected modes greatly enhance the image resolution relative to the direct mode alone. Calculations of vertical resolution based on the migration operators (Rondenay et al., 2005) suggest that the dominant back-scattered mode (*Ppxs*) should resolve features over scales of 4-6 km full-wavelength, while the direct wave has difficulty resolving features much smaller than 12-15 km full-wavelength (MacKenzie,

2008). Resolution degrades near the edge of the image and smearing becomes evident where azimuthal coverage becomes non-uniform.

Some obvious artifacts exist. Faint migration "smiles" can be seen below the subducting crust at depths of 60-100 km, perhaps disrupting it near 60-80 km depth, particularly in the *P*-wave image. These circular arcs centered on individual stations may reflect anomalous noise at those sites or otherwise incomplete coverage (Rondenay et al., 2005). Still, the geometry and strength of the low-velocity zone can be distinguished clearly, particularly in the upper 75 km. Mode separation tests (MacKenzie, 2008) show that the image is dominated by the first surface-reflected phase (*Ppxs*) for a variety of phase weightings, and that a projection azimuth of 100° provides the strongest image coherence so most likely represents the local downdip direction for the slab.

C. Hypocenter Relocations

A total of 28 earthquake hypocenters are relocated within the downgoing plate from regional arrival picks. These include all earthquakes Aug. 2006 – November 2007 at least 20 km deep and within 40 km of the projection line. Earthquakes have between 7 and 55 stations per event for a total of 907 *P* arrivals and 890 *S* arrivals. To aid comparison with the migration image they are relocated in the same one-dimensional velocity model (Supplementary Table S1) used in the migration, following standard methods (Abers and Roecker, 1991). Earthquakes with a formal 1-σ uncertainty in location exceeding 2 km are discarded.

Locations and depths of the three largest historical earthquakes occurring in 2001, 1965 and 1949 (moment magnitude = 6.6 – 6.8 for all) are taken from previously-published analyses of seismograms, based on picked depth phases (*pP*) or waveform inversion (Ichinose et al., 2004; Wiest et al., 2007). Although these particular studies do not estimate uncertainties in depth, typically such analyses provide depths accurate to a few km. The likely rupture dimension for these earthquakes (Ichinose et al., 2004) likely exceed 10 km, greater than the potential errors due to methodology, so reanalysis did not seem warranted.

D. Previous velocity constraints from tomography.

Several estimates exist of the *P*-wave velocity structure (*Vp*) beneath the northern Cascadia forearc, from local-earthquake and active-source tomography. Within 100 km of the coast, where the plate interface shows strong velocity contrasts (Figure 2, 3), three-dimensional *P*-wave traveltime inversions generally exhibit strong variability in upper-plate structure (Parsons et al., 1999; Preston et al., 2003; Ramachandran et al., 2006). Most show a "tongue" of low-velocity material overlying the plate at 20-35 km depth, with higher velocity material above, at least north of 47°N. The lower crustal rocks appear to have $Vp = 6.3 – 6.6$ km/s, while shallower velocities approach 7.0 km/s.

Initial analyses of *S* velocity structure (*V*s) from CAFE data via ambient noise tomography (e.g., Shapiro et al., 2005) indicates a *Vs* structure similar to the *Vp* structures obtained from body wave tomography (J. Calkins, pers. comm., 2009). These inversions show low velocities of $Vs = 3.3$-3.5 km/s at 20-35 km depth, and *Vs* as high as 3.8 km/s shallower. If these estimates are directly compared with body wave tomography, then they indicate $Vp/Vs = 1.80$-1.85 for the upper crust and 1.90-1.93 for the lower crust. These lower-crustal values are higher than expected for most silicic rocks (Christensen, 1996) and might be biased by resolution differences between the two methods, but the overall consistency in pattern between these independent data sets suggests overall consistency. As shown below, high *Vp/Vs* (1.90) agrees with CAFE receiver functions, although is substantially higher than estimated beneath Vancouver Island from receiver functions (Audet et al., 2009), perhaps indicating a substantial lithologic change along strike.

Within the mantle of the downgoing plate, body wave tomography consistently shows $Vp \geq 8.0$ km/s (Calvert et al., 2006; Parsons et al., 1999; Preston et al., 2003; Ramachandran et al., 2006), and ambient noise tomography (J. Calkins, pers. comm.) indicates $Vs \sim 4.6$ km/s. These velocities agree with expectations for anhydrous peridotites (see below) of $Vp \sim 8.1$ km/s and $Vp/Vs \sim 1.75$ at predicted temperatures.

Based on these studies, we approximate in analyses below the velocity of the overlying plate by $Vp = 6.5$ km/s and $Vs = 3.4$ km/s, while Juan de Fuca mantle velocities are assumed to be $Vp = 8.0$ km/s and $Vs = 4.6$ km/s. Small (<0.2 km/s) changes to these values, particularly to those for the underlying mantle, have no discernable effect on estimates for the intervening layers.

E. Velocity predictions for metasediments, metagabbros and peridotites.

It is possible that a thick section of terrigenous sediments are subducted at the top of the downgoing plate, creating low velocities. We examine here one endmember, in which all free fluids have been expelled, by calculating predicted velocities from the mineralogies of Hacker (2008) for two relevant analog compositions, an Alaska turbidite and Antilles terrigenous sediment. We also compare elastic properties measured experimentally in metasedimentary rocks (Takanashi et al., 2001) (Figure DR1). In the mineralogical predictions, metamorphic assemblages and elastic properties are calculated by the Perplex free-energy minimization (Connolly, 2005), following a pressure-temperature trajectory predicted for the top of the subducting plate in Cascadia (Rondenay et al., 2008). For comparison we calculate *Vp* and *Vs* expected for anhydrous harzburgite (DMM) and unreacting (metastable) gabbro with the same method; these compositions are expected in the underlying mantle and the coarse grained lower oceanic crust. Predicted metasediment velocities are significantly slower than those of metastable gabbro or eclogite at the depths of interest (<50 km), with $Vp = 6.3 – 6.7$ km/s and $Vs = 3.6 – 4.0$ km/s in metasediments, compared with gabbro velocities of $Vp = 7.2\text{-}7.3$ km/s, $Vs = 4.2$ km/s. However, these velocities are much higher than those measured experimentally in biotite-rich schists and gneisses of similar mineralogy (Takanashi et al., 2001). The elastic moduli for biotite in Perplex disagrees with some laboratory measurements (B. Hacker, pers. comm.), so the difference may be a problem with predictions, but the disagreement has not been thoroughly evaluated.

The direct rock measurements show 15-25% anisotropy in schists, indicated by the size of box B in Figure DR1. Slow directions of propagation for both *P* and *S* lie perpendicular to biotite foliation in these rocks (Takanashi et al., 2001), which might be expected to parallel the plate boundary shear zone at depth. Since the waves generating receiver functions propagate more normal to the thrust zone than along it, they probably sample the slow side of this velocity range, i.e., $Vp \sim 5.3\text{-}5.5$ km/s and $Vs \sim 2.8\text{-}3.0$ km/s. Vp/Vs varies highly between compositions, from 1.68 to 1.85. Thus, for reasonable fabric, foliated metasedimentary layers may exhibit much slower than average

wavespeeds by for near-vertical wave propagation. However, more work is needed to characterize elastic properties of sheet silicates and the fabrics they form.

F. Velocity estimates from receiver functions: data

Receiver function waveforms contain much information about structure, as summarized in Figure 3, and elaborated in the following section. All analyses are for stations 40 – 100 km from the coast (Figure 3), where both direct mode conversions (*Ps*) and first surface reverberations (*Ppxs*) can be identified (See Supplementary Section B for nomenclature). These phases should be of comparable amplitude. In most of these receiver function stacks, two conversions can be identified in both the *Ps* and *Ppxs* arrivals, a positive velocity step from the Juan de Fuca Moho and a shallower (shorter lag time) negative velocity step from the overlying plate interface. A later phase, *Psxs*, is present but interferes with late parts of *Ppxs* so is difficult to identify.

For simplicity we only analyze stacks of receiver functions from western back-azimuths (180-360°) as in Figure 3, bandpass filtered to 0.03 – 0.4 Hz or 0.03-0.5 Hz. Higher frequencies showed little coherent energy so could not be used. Effects of dip are expected to be minor, since the slab dips <10° here, and nearly identical results are obtained for different back-azimuth subsets, so effects of azimuthal anisotropy are not considered. The same signals are used in the detailed analyses below as shown in Figure 3.

G. Velocity estimates from receiver functions: analysis

We analyze velocity structure in two ways, from each receiver function. First, we determine layer thickness and *Vp/Vs* from picked lag times. Within both the *Ps* and *Ppxs* signals two phases can be seen, an earlier negative-amplitude arrival from the top of the low velocity layer and a later positive arrival from its base (Figure DR2). The difference between these positive-negative pairs provides an estimate of differential travel times within the layer, and when combined can be converted into estimates of layer thickness and *Vp/Vs*. This approach relies upon the same basic observations and theory as Audet et al. (2009) but is simpler in that we pick times of peaks rather than employ phase weighted stacking. A similar analysis of just the negative peaks provides an estimate of

depth to the plate boundary and *Vp/Vs* of the overlying crust (Zhu and Kanamori, 2000). One difficulty is that the positive-negative peak pairs are close in time and may interfere, especially for *Ps* (Audet et al., 2009), which may cause a bias toward large differential times for *Ps* and overestimates of *Vp/Vs*. We have tried a range of low-pass filter frequencies from 0.2 to >0.5 Hz and see a correlation of filter frequency with calculated *Vp/Vs* throughout the range. At frequencies >0.5 Hz the arrivals cannot be uniquely identified or little energy arrives, limiting the minimum layer thickness over which unbiased results can be obtained.

The second approach is to model and invert the waveforms directly, using a parameterization of structure with a relatively few number of free parameters. By filtering model and data identically, phase interference biases can be avoided. The model assumes four layers, a continental crust, low-velocity plate boundary, subducting oceanic crust, and oceanic mantle. Based on the results of sections D and E above we fix velocities for the mantle, continental crust, and *Vp/Vs* for oceanic crust (assuming it is gabbroic). We also fix the thickness of the oceanic crust to 7 km. All other parameters are adjusted by Nelder-Mead nonlinear minimization to find a best fit to the first 40 s of the receiver functions; an example is shown in Figure DR3. Several starting models and filter frequencies were tested, along with back-azimuth bins.

In general, models reconstruct well the increasing slab depth with distance from coast (Figure DR4c) and both methods confirm low velocity zones of a few km. The picking method overestimates *Vp/Vs* relative to waveform modeling, perhaps due to filtering bias. The waveform inversion method only shows good fits when the low-velocity zone consists of two (or more) layers, with the lower layer *Vp* near 6.7 - 7.0 km/s (compare Figures DR4a, DR4b with Figure DR1). The upper layer is much slower, with *Vp* ~ 5.0± 0.3 km/s and *Vs* ~ 2.6 ± 0.3 km/s (*Vp/Vs* ~ 1.9), and is 2.5-5.5 km thick. To first order, the amplitudes of the conversions control the velocities, while thicknesses and *Vp/Vs* depend upon their timing.

The upper-layer velocities are lower than the velocities for metasediments predicted (*Vp*=6.3-6.7 km/s) or measured in laboratory (5.3-6.3 km/s), and *Vp/Vs* is higher. This would indicate that composition alone is insufficient to explain the high amplitude receiver functions, and that elevated fluid pressures may be needed, but much

less would be needed than were the host rock basaltic in composition. Pore fluids would be needed to reduce *Vp* by 0.3-1.5 km/s, and increase *Vp/Vs* by perhaps only 0.05.

H. Relationship between intraslab earthquakes and oceanic Moho.

Several tests were done to confirm that intraslab earthquakes lie below the slab Moho as appears in Figure 2 (MacKenzie, 2008). In Figure 2, seismicity averages 5.4 km deeper than the oceanic crust at depths < 50 km, and 7.3 km deeper than it at greater slab depths. In all tests, the velocity structure used to locate earthquakes is the same as that used in the migration. Earthquakes are located largely by the same stations, *P* and *S* arrivals from them recorded at CAFE stations were picked and weighted strongly in the location, so that near-site effects should have similar effects. In this way any systematic effects due to shallow structure should be minimized. This process was repeated in several velocity models – the model used to locate earthquakes by the regional network there, the model used to migrate the Oregon scattered wave data (Bostock et al., 2002), and models in which the ratio *Vp/Vs* was perturbed by ±0.05. Larger shifts to velocity are not warranted, given the existing velocity constraints (see Section D above). In all cases, the earthquakes lie beneath the Moho, although the mean difference varies by 2-3 km. For an Alaska data set with similar ray geometries, Monte Carlo simulations confirm similar levels of robustness of the relationship between seismicity and imaged structures (Abers et al., 2006). Finally, the projection azimuth was varied at 10° intervals from 80° to 130°. For all rotations, seismicity was deeper than the Moho, so the relationship is not an artifact of projection.

Supplementary Table DR1. One-dimensional velocity model used for migration and hypocenters

Depth* (km)	*Vp* (km/s)	*Vs* (km/s)	Density (g/cm^3)
0	5.40	3.09	2.6
4	6.38	3.65	2.6
9	6.59	3.77	2.8
16	6.73	3.85	3.1
20	6.86	3.92	3.1
25	6.96	3.98	3.1
41	7.8	4.46	3.5

*Velocities and density are constant below each listed depth.

SUPPLEMENTARY MATERIAL: REFERENCES

Abers, G.A., and Roecker, S., 1991, Deep structure of an arc-continent collision: earthquake relocation and inversion for upper mantle P and S wave velocities beneath Papua New Guinea: J. Geophys. Res., v. 96, p. 6379-6401.

Abers, G.A., van Keken, P.E., Kneller, E.A., Ferris, A., and Stachnik, J.C., 2006, The thermal structure of subduction zones constrained by seismic imaging: implications for slab dehydration and wedge flow: Earth Planet. Sci. Lett., v. 241, p. 387-397.

Audet, P., Bostock, M.G., Christensen, N.I., and Peacock, S.M., 2009, Seismic evidence for overpressured subducted oceanic crust and sealing of the megathrust: Nature, v. 457, p. 76-78.

Bostock, M.G., and Rondenay, S., 1999, Migration of scattered teleseismic body waves: Geophys. J. Int., v. 137, p. 732-746.

Bostock, M.G., Rondenay, S., and Shragge, J., 2001, Multiparameter two-dimensional inversion of scattered teleseismic body waves; 1, Theory for oblique incidence: J. Geophys. Res., v. 106, p. 30,771-30,782.

Bostock, M.G., Hyndman, R.D., Rondenay, S., and Peacock, S.M., 2002, An inverted continental Moho and serpentinization of the forearc mantle: Nature, v. 417, p. 536-538.

Calvert, A., Ramachandran, K., Kao, H., and Fisher, M.A., 2006, Local thickening of the Cascadia forearc crust and the origin of seismic reflectors in the uppermost mantle: Tectonophysics, v. 420, p. 175-188.

Christensen, N.I., 1996, Poisson's ratio and crustal seismology: J. Geophys. Res., v. 101, p. 3139-3157.

Connolly, J.A.D., 2005, Computation of phase equilibria by linear programming: a tool for geodynamic modeling and its application to subduction zone decarbonation: Earth Planet. Sci. Lett., v. 236, p. 524-541.

Hacker, B.R., 2008, H2O subduction beyond arcs: Geochem. Geophys. Geodyn. (G3), v. 9, p. Q03001, doi:10.1029/2007GC001707.

Ichinose, G.A., Thio, H.K., and Somerville, P.G., 2004, Rupture process and near-source shaking of the 1965 Seattle-Tacoma and 2001 Nisqually, intraslab earthquakes: Geophys. Res. Lett., v. 31, p. art. no. L10604.

Kennett, B.L.N., 1991, Removal of free surface interactions from three-component seismograms: Geophys. J. Int., v. 104, p. 153-163.

Ludwin, R.S., 1994, Earthquake hypocenters in Washington and northern Oregon, 1987-1989, and Operation of the Washington Regional Seismograph Network: Seattle, Washington State Dept. Nat. Res.

MacKenzie, L.S., 2008, A Receiver Function Study of the Central America and Cascadia Subduction Zone Systems, PhD Thesis [Ph.D. Thesis thesis], Boston Univ.

Parsons, T., Wells, R.E., Fisher, M.A., Flueh, E., and ten Brink, U.S., 1999, Three-dimensional velocity structure of Siletzia and other accreted terranes in the Cascadia forearc of Washington: J. Geophys. Res., v. 104, p. 18015-18039.

Pisarenko, V.F., Kushnir, A.F., and Savin, I.V., 1987, Statistical adaptive algorithms for estimation of onset moments of seismic phases: Phys. Earth and Planet. Int., v. 47, p. 4-10.

Preston, L.A., Creager, K.C., Crosson, R.S., Brocher, T.M., and Trehu, A.M., 2003, Intraslab earthquakes: dehydration of the Cascadia slab: Science, v. 302, p. 1197-2000.

Ramachandran, K., Hyndman, R.D., and Brocher, T.M., 2006, Regional P wave velocity structure of the Northern Cascadia Subduction Zone: J. Geophys. Res., v. 111, p. art no. B12301.

Rondenay, S., Bostock, M.G., and Fischer, K.M., 2005, Multichannel inversion of scattered teleseismic body waves: practical considerations and applicability, *in* Levander, A., and Nolet, G., eds., Seismic Earth: Array Analysis of Broadband Seismograms Volume 157: Geophys. Monogr. Ser.: Washington, Amer. Geophys. Un., p. 280pp.

Rondenay, S., Abers, G.A., and van Keken, P.E., 2008, Seismic imaging of subduction zone metamorphism: Geology, v. 36, p. 275-278.

Shapiro, N.M., Campillo, M., Stehly, L., and Ritzwoller, M.H., 2005, High-resolution surface-wave tomography from ambient seismic noise: Science, v. 307.

Takanashi, M., Nishizawa, O., Kanagawa, K., and Yasunaga, K., 2001, Laboratory measurements of elastic anisotropy parameters for the exposed crustal rocks from the Hidaka Metamorphic Belt, Central Hokkaido, Japan: Geophys. J. Int., v. 145, p. 33-47.

VanDecar, J.C., and Crosson, R.S., 1990, Determination of teleseismic relative phase arrival times using multi-channel cross-correlation and least squares: Bull. Seismol. Soc. Amer., v. 80, p. 150-159.

Wech, A.G., and Creager, K.C., 2008, Automated detection and location of Cascadia tremor: Geophys. Res. Lett., v. 35, p. L20302, doi:10.1029/2008GL035458.

Wech, A.G., Creager, K.C., and Melbourne, T.I., 2008, Seismic and geodetic constraints on slow slip in Cascadia: J. Geophys. Res., v. submitted.

Wiest, K.R., Doser, D.I., Velasco, A.A., and Zollweg, J., 2007, Source investigation and comparison of the 1939, 1946, 1949 and 1965 earthquakes, Cascadia subduction zone, Western Washington: Pure and App.. Geophys., v. 164, p. 1905-1919.

Zhu, L., and Kanamori, H., 2000, Moho depth variation in Southern California from teleseismic receiver functions: J. Geophys. Res., v. 105, p. 2969-2980.

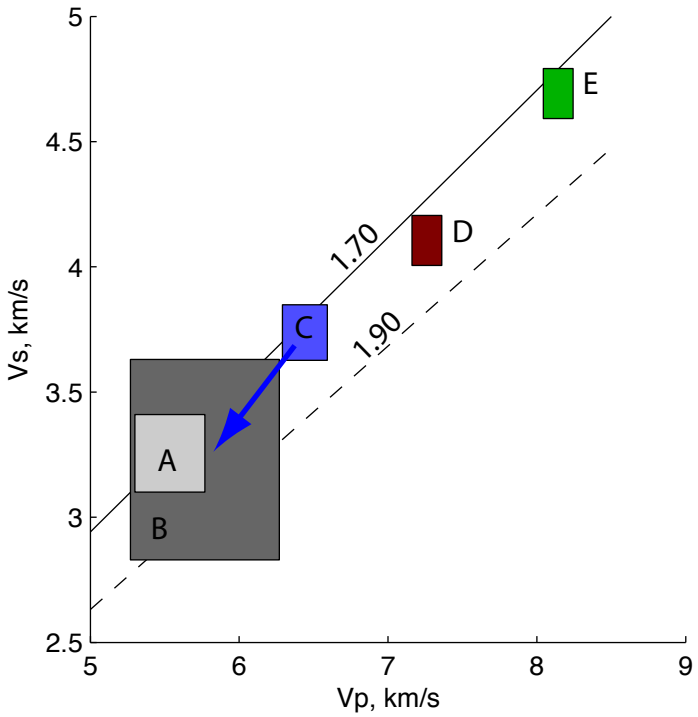

Figure S1. Predicted P and S velocities for metasediments and other relevant compositions. (A) and (B) are measured velocities in (A) biotite gneiss SB-7 and (b) biotite schist ST-3 from Takanashi et al. (2001); width of box shows range produced by anisotropy over all propagation and polarization directions. Samples measured at 150 MPa, with 34-36 % biotite, slow propagation is generally perpendicular to foliation. (C) Predicted metasedimentary compositions from calculations of Hacker (2008) for Alaska turbidite and Antilles terrigenous sediment, at P-T conditions corresponding to 20-40 km depth along the Cascadia slab, from thermal models (Rondenay et al., 2008). Elastic moduli may be significantly overestimated for micas (B. Hacker, pers. comm.), by ~ 0.5 km/s in velocity. (D) Predictions for metastable gabbro from Hacker (2008) at same P-T conditions as C. (E) Predictions for dry peridotite, similar to C and D. For D and E, box width reflects a nominal 0.1 km/s uncertainty. Lines indicate constant Vp/Vs (or Poisson) ratio, as labeled.

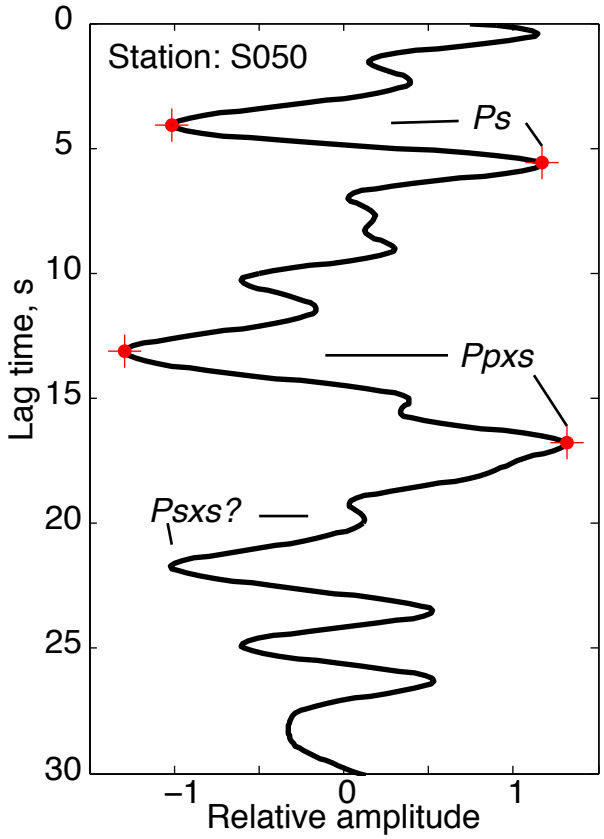

Figure DR2. Example of picking lag times to determine structure, from stacked trace of station S050 (rightmost on Figure 3). Receiver functions are stacked as described in text, then bandbass filtered at 0.03 - 0.4 Hz. Four dots/crosses show peaks corresponding to Ps and Ppxs, for top and bottom of low velocity layer. The first Psxs phase is difficult to identify, and may interfere with late parts of Ppxs. Analysis of these times gives a low velocity layer 5.9 km thick with Vp/Vs = 2.16 and an upper-plate crust 33.4 km thick and with Vp/Vs = 1.85, assuming Vp = 5.0 km/s and 7.0 km/s respectively.

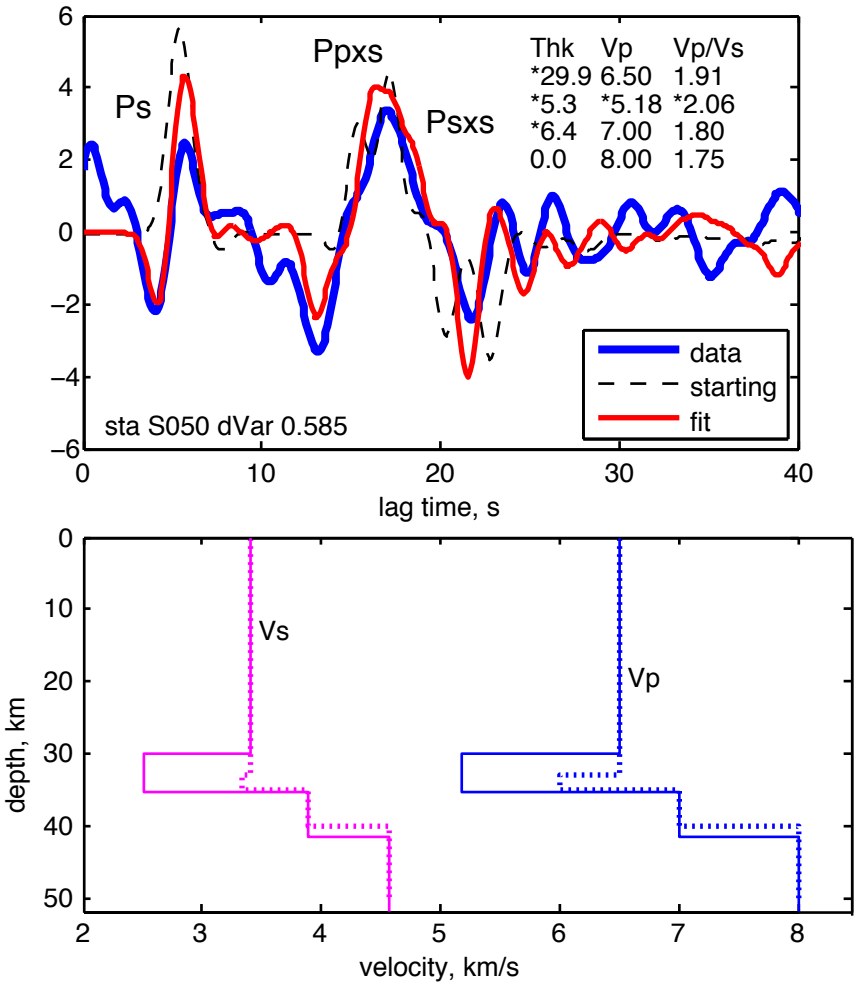

Figure DR3. Example of waveform inversion for properties of low-velocity zone, for CAFE station S050 (rightmost trace in Figure 3). (Top) Receiver functions and models. Blue line shows observed receiver functions, stacked as in Figure 3, but filtered 0.03-0.5 Hz. Dashed line shows starting model for inversion, red shows best fit, for 58.5% variance reduction. Table in upper right shows layer thickness (km), Vp, and Vp/Vs for best fit model, parameters denoted "*" are free in the inversion. (Bottom) starting (dashed) and final (solid) velocities. The strong negative pulse in both Ps and Ppxs requires a sharp velocity reversal at 30 km depth.

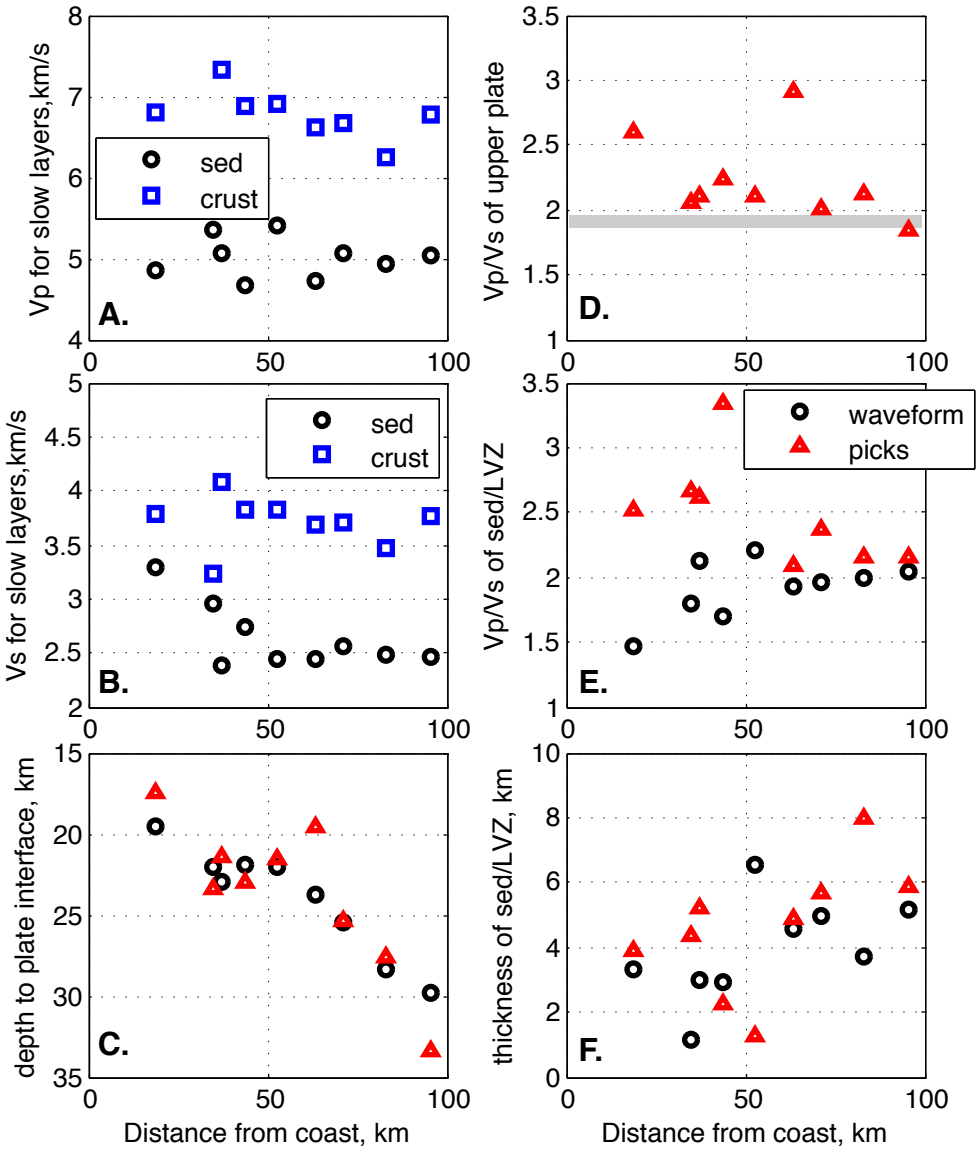

Figure DR4. Results from inversions for structure from single-station stacked receiver functions. Stations correspond to those in Fig. 3, plotted vs. distance from coast. A. Vp from waveform inversion, for two layers within low-velocity zone. B. Vs from waveform inversion, for two layers within low-velocity zone. C. Depth to top of low-velocity layer, from waveform inversion (circles) and from picked times (triangles). D. Vp/Vs ratio for upper plate from picked arrivals; gray bar shows estimate from previous tomographic studies. E. Vp/Vs for low-velocity zone from picked arrivals (triangles) or from upper sediment layer based on waveform inversion (circles). F. Thickness of low-velocity zone from picked arrivals (triangles) or of sediment from waveform inversion (triangles). In general, Vp/Vs from picked arrivals is higher than from other methods, perhaps because of bias due to interferences between negative and positive picks. All methods accurately show slab deepening away from coast (C.), and indicate high (>1.8) Vp/Vs ratios for low velocity zone.